Fast EVP solutions in a high-resolution sea ice model

Nikolay V. Koldunov[1,2], Sergey Danilov[2,3,4], Dmitry Sidorenko[2], Nils Hutter[2], Martin Losch[2], Helge Goessling[2], Natalja Rakowsky[2], Patrick Scholz[2], Dmitry Sein[2,5], Qiang Wang[2]and Thomas Jung[2,6]

[1]MARUM - Center for Marine Environmental Sciences, Bremen,Germany.
[2]Alfred-Wegener-Institut, Helmholtz Zentrum für Polar- und Meeresforschung, Bremerhaven, Germany.
[3]Department of Mathematics and Logistics, Jacobs University, Bremen, Germany.
[4]A. M. Obukhov Institute of Atmospheric Physics RAS, Moscow, Russia.
[5]P. P. Shirshov Institute of Oceanology RAS, St. Petersburg, Russia.
[6]Institute of Environmental Physics, University of Bremen, Bremen, Germany.

Key Points:

- We explore the performance of new options for EVP solvers at high resolution (4.5 km).
- A significant reduction of the required number of EVP sub-cycles leads to a 6-fold speed-up of the sea ice dynamics.
- This speed-up does not lead to a deterioration of the simulated sea ice.

Corresponding author: Nikolay V. Koldunov, `nikolay.koldunov@awi.de`

Abstract

Sea ice dynamics determine the drift and deformation of sea ice. Non-linear physics, usually expressed in a viscous plastic rheology, make the sea ice momentum equations notoriously difficult to solve. At increasing sea ice model resolution the non-linearities become stronger as linear kinematic features (leads) appear in the solutions. Even the standard elastic-viscous-plastic (EVP) solver for sea ice dynamics, which was introduced for computational efficiency, becomes computationally very expensive, when accurate solutions are required, because the numerical stability requires very short, and hence more, sub-cycling time steps at high resolution. Simple modifications to the EVP solver have been shown to remove the influence of the number of sub-cycles on the numerical stability. At low resolution appropriate solutions can be obtained with only partial convergence based on a significantly reduced number of sub-cycles as long as the numerical procedure is kept stable. This previous result is extended to high resolution where linear kinematic features start to appear. The computational cost can be strongly reduced in Arctic Ocean simulations with a grid spacing of 4.5 km by using modified and adaptive EVP versions because fewer sub-cycles are required to simulate sea ice fields with the same characteristics as with the standard EVP and large numbers of sub-cycles.

1 Introduction

Most sea ice models use a viscous-plastic (VP) rheology [*Hibler*, 1979] to describe internal stresses in the sea ice pack. This entails numerical difficulties related to the stiff character of the corresponding momentum equations so that explicit solution methods are unacceptably expensive. There are two strategies to overcome these difficulties. One resorts to implicit methods, requiring numerical solvers. Implicit methods range from approximate solutions where only a few Picard iterations are performed [*Zhang and Hibler*, 1997], to sophisticated solvers, such as the Jacobian-free Newton–Krylov (JFNK) solver [*Lemieux et al.*, 2012, *Losch et al.*, 2014], which ensure numerical convergence of solutions to the dynamical equations. In practice, however, the JFNK solver is still computationally expensive and up to now rather serves as a tool for providing reference solutions of the dynamical sea ice equations.

The other strategy is to add pseudo-elasticity to the governing VP equations (see the Appendix for a list of relevant equations). This makes the dynamical equations second-order with respect to time and reduces time-step limitations. This so-called elastic-viscous-plastic (EVP) method [*Hunke and Dukowicz*, 1997] is widely used in numerical climate modeling.

The applicability of the VP rheology for the representation of sea ice, especially at high resolution, is criticized in the literature since for many assumptions this rheology uses there is no observational evidence [see e.g. *Weiss et al.*, 2007, *Coon et al.*, 2007, *Rampal et al.*, 2008]. Many modifications of the VP rheology that should better reflect some of the properties of sea ice were suggested [e.g. *Hibler and Schulson*, 2000, *Zhang and Rothrock*, 2005, *Tremblay and Mysak*, 1997, *Tsamados et al.*, 2013]. More fundamentally different rheologies are also in development [*Girard et al.*, 2011, *Rampal et al.*, 2016, *Dansereau et al.*, 2016], as are discontinuous discrete element approaches which resolve individual floes [e.g. *Hopkins*, 2004, *Wilchinsky and Feltham*, 2012, *Herman*, 2011]. A more detailed list of new approaches to model sea ice dynamics can be found in *Ringeisen et al.* [2018].

Still, most of the climate models participating in CMIP use some form of VP rheology, and most often in its EVP form [*Stroeve et al.*, 2014]. Reasons include the relatively good performance when compared to observations, even in high-resolution configurations with up to 1km grid spacing [*Wang et al.*, 2016a, *Hutter et al.*, 2018a, *Spreen et al.*, 2017, *Bouchat and Tremblay*, 2017], and better computational performance when compared to other attempts to simulate sea ice on the global scale. In practice, this means that EVP will continue to be used widely for climate research for the next several years before better alternatives in terms of both computational performance and comparison to observations are developed.

Because EVP method is explicit in time, it requires sub-cycling within the external time step of the sea ice or ocean circulation model. The number of sub-cycles (N_{EVP}) depends on the grid resolution [*Hunke and Dukowicz*, 1997]. From stability analysis it becomes clear that N_{EVP} can reach several hundreds at high resolution. With very high resolution on the order of one kilometer, sea ice dynamics can become as expensive as the entire ocean model (Fig. 1). Too small N_{EVP} may lead to numerical noise [see e.g. *Losch and Danilov*, 2012, *Lemieux et al.*, 2012, *Bouillon et al.*, 2013], which changes the structure of the simulated ice distribution [see e.g. *Wang et al.*, 2016a]. Furthermore, even though EVP was designed to do so, EVP solutions were found to generally not converge to a VP solution [*Losch et al.*, 2010, *Losch and Danilov*, 2012, *Lemieux et al.*, 2012].

In recognizing especially the last point, *Lemieux et al.* [2012] and later *Bouillon et al.* [2013], *Kimmritz et al.* [2015] reformulated EVP as a pseudo-time iterative process that guarantees convergence to the VP solution by construction. Importantly, the new procedure separates the issue of numerical stability from the number of sub-cycles N_{EVP}. The latter is still responsible for the degree of convergence whereas the numerical stability is governed only by two parameters α and β (see the Appendix for definitions). A careful analysis of numerical stability and convergence properties of the scheme [*Kimmritz et al.*, 2015] lead to a further modification where the stability is taken into account in an automatic, adaptive way [*Kimmritz et al.*, 2016]. Following the terminology of *Kimmritz et al.* [2016], the "revised" approach with constant α and β [*Bouillon et al.*, 2013] will be referred to as mEVP ("m" for modified), and its adaptive version as aEVP.

The performance of mEVP and aEVP was compared to that of a JFNK solver in a realistic Arctic configuration on a mesh with a resolution of approximately 27 km [*Kimmritz et al.*, 2017]. Both algorithms produced results very similar to that simulated by the JFNK solver, except in the marginal ice zone where the sea ice is in free drift and the solver characteristics are not important, but where advective processes and ice-ocean feedbacks make the system more chaotic. It was found that both mEVP and aEVP solvers work reasonably well with much lower N_{EVP} than recommended for the traditional EVP solver [e.g. the CICE manual recommends 120 sub-cycles, *Hunke et al.*, 2010]. The distributions of ice thickness and strain rates simulated with N_{EVP} equal to 50 and 250 remain rather close to each other and deviate little from the JFNK result. The value of N_{EVP}=250 satisfies the formal condition for convergence since it is close to the stability parameters α and β, but N_{EVP}=50 is formally too small to ensure convergence within the external time step. Because each EVP iteration is started from the result of the previous time step, however, this number proves to be sufficient to maintain convergence through the integration, presumably achieved gradually on a long time scale. This finding opens a perspective to reduce the numerical cost substantially if mEVP or aEVP solvers are used in place of EVP [*Kimmritz et al.*, 2017].

Sea ice thickness and concentration simulated at 27 km resolution are smooth. VP sea ice dynamics start to reveal multiple linear kinematic features (leads, or openings) as the grid spacing is reduced to 5 km or lower [*Wang et al.*, 2016a, *Hutter et al.*, 2018a], and the conclusion that mEVP and aEVP can be run with much smaller N_{EVP} than formally required by the standard EVP for such type of resolutions may not necessarily be valid [*Kimmritz et al.*, 2017].

In this paper, we use FESOM2 [*Danilov et al.*, 2017] with FESIM [*Danilov et al.*, 2015] as the sea ice component, which includes both mEVP and aEVP. The model is run in a global configuration with uniform refinement to 4.5 km in the entire Arctic Ocean. This mesh has been used in FESOM simulations for Arctic Ocean studies *Wang et al.* [2018a,b, 2019]. Its resolution already allows to simulate numerous linear kinematic features (LKF) in the sea ice field [*Wang et al.*, 2016a]. Here we explore the extent to which N_{EVP} can be reduced without degrading the obtained solutions; and it turns out that even in this case the values as low as $N_{EVP} = 100$ appear acceptable.

We stress that we focus only on the impact of the sea ice solver in the regionally refined Arctic Ocean. We do not explore the sensitivity to other parameters and do not compare results to observations. This study can be considered as an example of the mEVP and aEVP sea ice model tuning procedure for high-resolution applications.

FESIM does not have a JFNK solver, so we cannot explore how its mEVP and aEVP solutions deviate from fully converged solutions, let alone possible difficulties in reaching convergence with a JFNK solver in the presence of numerous LKFs [*Losch et al.*, 2014]. Fully converged JFNK solutions only differ from the mEVP and aEVP solutions with a relatively low N_{EVP} in details that are not important for most practical applications [*Kimmritz et al.*, 2017]. Relying on this, we compare the EVP options with varying N_{EVP} in practically feasible limits. We concentrate on a realistic setting and try to minimize the computational cost under the condition of getting practically acceptable solutions.

The manuscript is organized as follows: In Section 2 we describe model, methods and software used for the analysis. In Section 3 we discuss the model performance and results for the unmodified EVP, in Section 4 we present results for mEVP and in Section 5 for aEVP. Summary and concluding remarks are provided in Section 6.

2 Model description and methods

The Finite volume sea ice ocean model [FESOM2, *Danilov et al.*, 2017] is the successor of FESOM1.4 [*Wang et al.*, 2014], a global ocean model that uses unstructured meshes. Due to a new dynamical core, FESOM2 is up to five times faster than FESOM1.4. A triangular mesh allow one to distribute horizontal resolution in the global model accord-

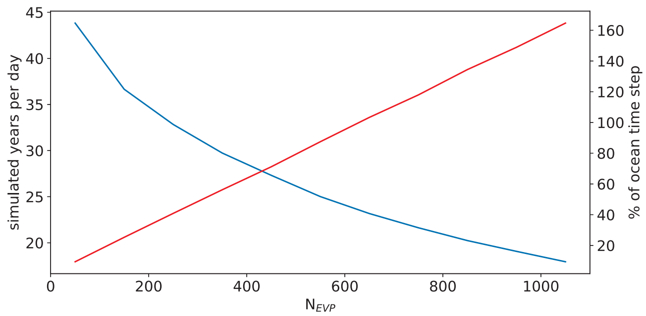

Figure 1. Throughput for FESOM2 simulations on a global mesh with 4.5 km Arctic Ocean with different values of N_{EVP} in the sEVP solver on 1728 Cores of a Cray CS400 with Intel®Xeon®Broadwell E5-2697 2.3 GHz 18Core CPUs (blues line) and percent of ocean time step required to calculate sea ice time step for different values of N_{EVP} (red line).

ing to some “resolution function" [*Sein et al.*, 2016, 2017] or by “zooming" into a specific region of interest [*Wekerle et al.*, 2017a,b] without traditional nesting.

In this paper we use a mesh with a 4.5 km horizontal grid spacing (defined as the length of the triangle sides) in the Arctic Ocean and an equivalent of 1 degree resolution in the rest of the globe [*Wang et al.*, 2018a]. The mesh has 47 unevenly spaced vertical layers. The vertical mixing parameterization is KPP [*Large et al.*, 1994]. Isoneutral diffusion [*Redi*, 1982] and the GM parameterization [*Gent and Mcwilliams*, 1990] are used. The GM coefficient is set to zero when the horizontal grid spacing becomes smaller than 25km, so that GM is not active in the Arctic Ocean.

Most of the model parameters in our runs are the same as those of *Wang et al.* [2018a]. The transition from FESOM1.4 to FESOM2, however, leads to some modifications in the ocean circulation, which will be reported in a dedicated ocean model evaluation paper.

The sea ice model component is version 2 of the Finite Element Sea Ice Model [FESIM, *Danilov et al.*, 2015]. It uses zero-layer thermodynamics [*Semtner Jr*, 1976] and includes several variants of an EVP solver. The “standard” EVP solver (sEVP) is based on *Hunke and Lipscomb* [2008], but contains a small but important adjustment in the stress evolution equations [*Bouillon et al.*, 2013, *Danilov et al.*, 2015] that reduces the noise in the velocity derivatives. For convenience, the equations and parameters of sEVP, mEVP, and aEVP are briefly described in Appendix A.2 and A.4. The sEVP version was used to investigate spatial and temporal variability of lead area fraction in the Arctic Ocean with FESOM1.4 [*Wang et al.*, 2016a]. In FESOM, the sea ice model is run on the same CPUs as the ocean. The external time step of the sea ice model is that of the ocean model.

To generate a base-line experiment the model was initialized in the year 1948 with PHC climatology [*Steele et al.*, 2001] and run with COREII forcing [*Large and Yeager*, 2009] until the year 2007. During this experiment, sEVP with $N_{EVP} = 50$ was used. All the following experiments were started from a restart file of the baseline experiment on 1 January 1980 and run for 10 years until 31 December 1989.

We detect LKFs from sea ice thickness fields with an LKF detection algorithm [*Hutter et al.*, 2018b] that (i) classifies pixels that have a lower thickness compared to the local surroundings as pixels of LKFs, (ii) separates the binary LKF map into small segments, and (iii) connects multiple segments to individual LKFs based on a probability that is determined by their distance and orientation relative to each other. The introduction of the probability-based reconnection improves the performance of the original algorithm of *Linow and Dierking* [2017].

Data analysis and visualization were performed with the following python packages: matplotlib [*Hunter*, 2007], Jupyter [*Kluyver et al.*, 2016], xarray [*Hoyer and Hamman*, 2017], pandas [*McKinney*, 2010] and scikit-image [*Van der Walt et al.*, 2014].

3 sEVP simulations

A series of sEVP experiments was carried out with the number of sub-cycles (N_{EVP}) increasing from 50 to 1050 with steps of 100. In the following we first describe the model's computational performance obtained in these experiments and then discuss their results.

3.1 Computational performance

Compared to *Hunke and Lipscomb* [2008], the sEVP algorithm in FESOM is slightly modified (Appendix A.2). Only with this modification it was possible to simulate linear kinematic features in the sea ice at all, albeit with a sufficiently large number of sub-cycles [*Wang et al.*, 2016a]. Larger values of N_{EVP} naturally decrease the model throughput. The baseline simulation with N_{EVP}=50 reaches about 43 simulated years per day (Fig. 1), with the sea ice code using only about 10% of the time needed by the ocean component. With $N_{\mathrm{EVP}} = 350$, LKFs only begin to appear in the solutions (see Fig. 2

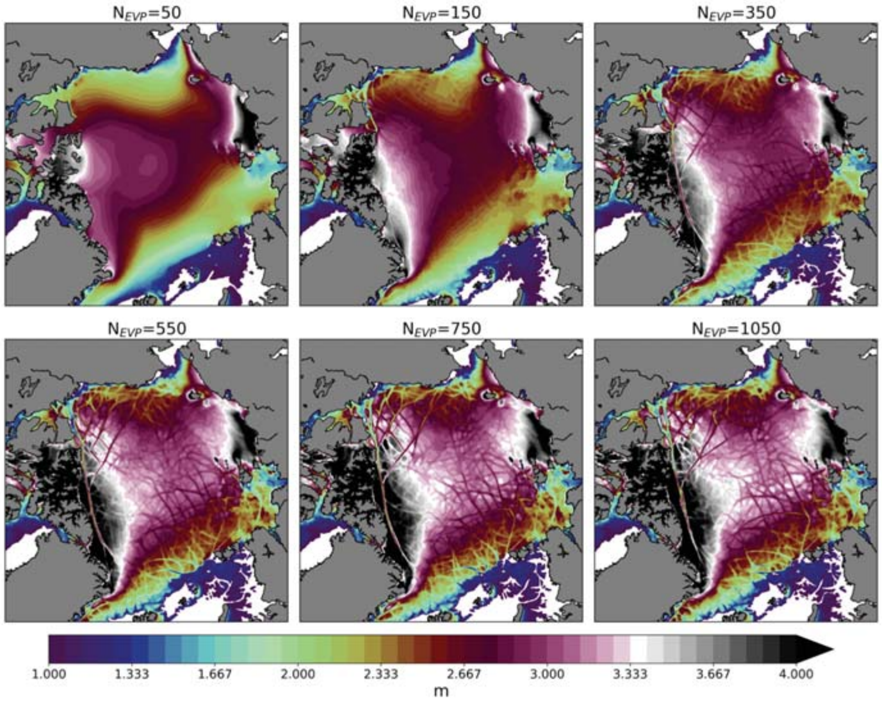

Figure 2. Snapshot of sea ice thickness on 31 December 1985 in sEVP simulations with different values of N_{EVP}. Only six of the experiments are shown.

in Section 2), but the model throughput drops to 30 simulated years per day and the sea ice code takes about 50% of the computational time needed for the ocean. With N_{EVP} = 650, the amount of CPU time needed for ocean and sea ice is almost the same and the throughput drops further to 23 simulated years per day. Taking N_{EVP} = 550 as the reference value generally needed for reducing the noise in the deformation fields on this mesh, it is clear that with the sEVP approach simulations of realistic sea ice dynamics on a high-resolution mesh require considerable computing resources, comparable to the resources required by the 3D ocean model.

3.2 sEVP results

The sea ice thickness field is very smooth for N_{EVP} = 50 and starts to develop some openings in the sea ice only with about N_{EVP} = 350 sub-cycles (Fig. 2). The solutions with N_{EVP}=550, 750 and 1050 look very similar to each other.

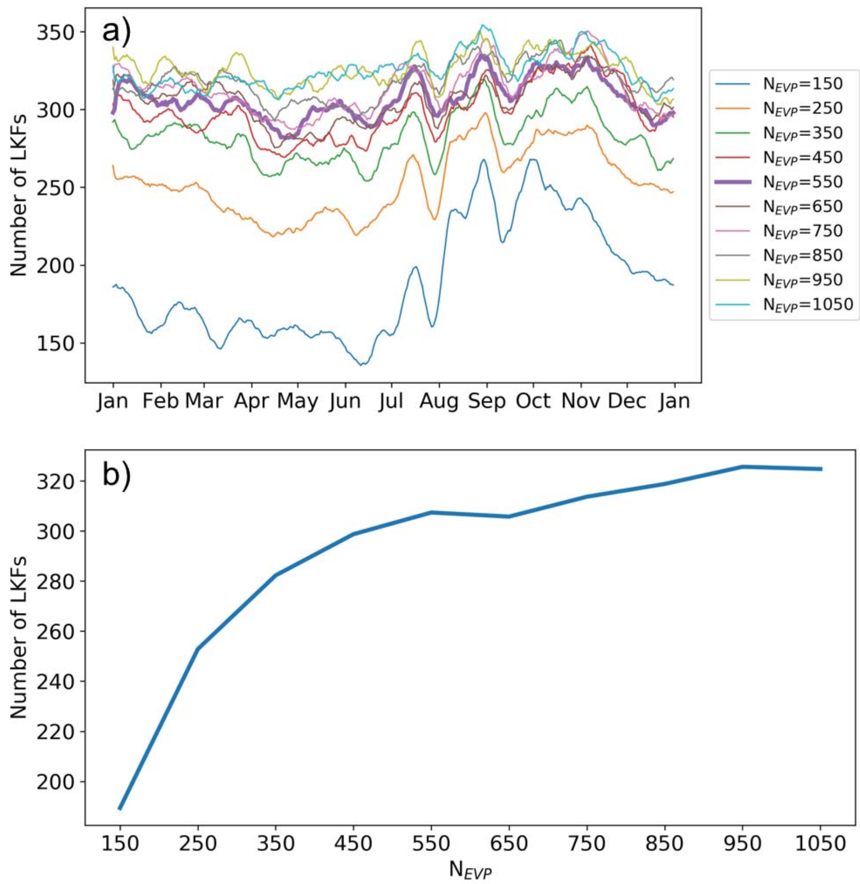

Figure 3. Number of LKFs for simulations with different values of N_{EVP} in sEVP simulations for the year 1986 (top). A 10-days running mean is applied to the time series. The thicker magenta line corresponds to the simulation with N_{EVP} = 550. The yearly mean number of LKFs with respect to N_{EVP} (bottom).

The appearance of LKFs is the most striking feature as N_{EVP} increases. The simulated LKFs introduce anisotropy into the pack ice although by definition the ice within one grid cell is isotropic. For a more elaborate study and evaluation of simulated LKFs and their impact on sea-ice deformation we refer to *Hutter et al.* [2018a], *Spreen et al.* [2017], *Wang et al.* [2016a].

We compare the number of LKFs in different solutions (Fig. 3). The LKFs are detected in daily sea ice thickness fields of the year 1986 (Fig. 3a). With increasing N_{EVP} the number of LKFs initially increases rapidly, but levels off around N_{EVP} = 550. This is especially clear for the annual mean number of LKFs (Fig. 3b). More sub-cycles mean a

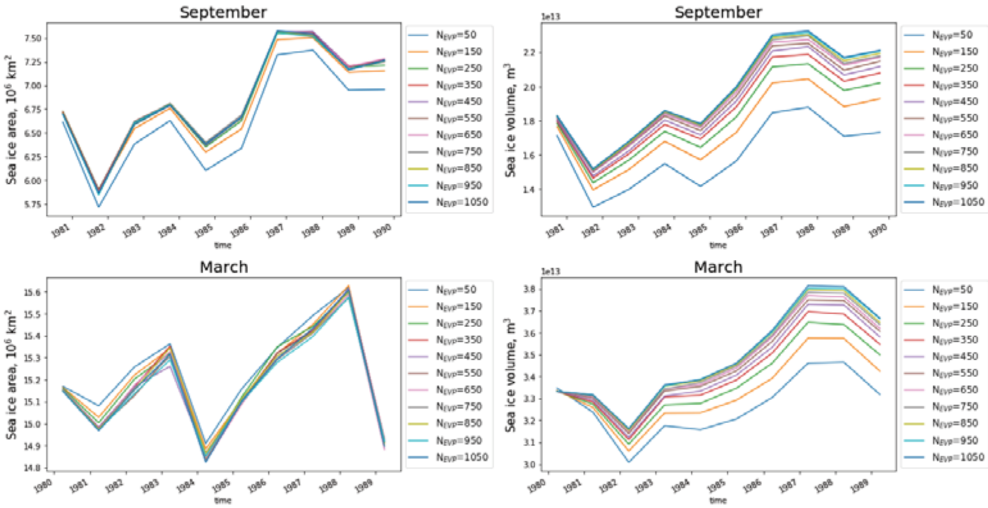

Figure 4. Monthly mean September (top) and March (bottom) Arctic sea ice area (left) and volume (right) in sEVP simulations with different values of $\mathrm{N_{EVP}}$.

considerable increase in computer resources (Fig. 1), but for N_{EVP} >550 the total number of LKFs does not increase very much, so that $N_{\mathrm{EVP}} = 550$ with ~ 300 LKFs appears to be a good compromise between the number of generated LKFs and the computational cost in this 4.5 km configuration. An LKF data-set based on satellite observations finds numbers of ~ 250 LKFs in the Western Arctic for the winters from 1997 to 2008 [*Hutter et al.*, 2018b]. If we consider that this data-set covers only 65 % of the model domain, we obtain a reference of ~ 380 LKFs that is not reached by any of our choices for N_{EVP}.

The changing structure of the sea ice fields also modifies integral sea ice properties such as Arctic sea ice area (SIA) and sea ice volume (SIV) (Fig. 4, 5). The time series of mean September and March SIA and SIV show positive trend over 1980-1989 period, in contrast to observations. This is due to generally overestimated sea ice extent and exaggerated interannual variability that is similar to other sea-ice ocean models participated in CORE-II intercomparison experiment [*Wang et al.*, 2016b].The SIA time series are not affected very much by the number of sub-cycles, except for very small numbers of $N_{\mathrm{EVP}} = 50$ and $N_{\mathrm{EVP}} = 150$. The low sensitivity of SIA to changes in the details of the sea ice thickness distribution is most probably related to the fact that the sea ice coverage is to a large extent already predefined by the forcing fields [e.g. *Koldunov et al.*, 2010, *Ernsdorf et al.*, 2011].

Similarly to the number of LKFs, the SIV increases with N_{EVP} especially for small N_{EVP}. The response of the SIV to changes in the value of N_{EVP} is stronger when the value is small. Possible explanations for such a sensitivity are the increasing amount of open water in leads due to more LKFs, or changes in the ice velocities and modified dynamics of ridging as N_{EVP} increases. New sea ice is actively formed in newly opened leads and also rafts and piles up when the ice cover is closing. *Kwok* [2006] used satellite data to estimate the relationship between sea ice deformation rates and sea ice growth. He found that higher and more active deformation is associated with higher ice production and estimated that seasonal ice growth in ice fractures accounts for 25-40% of the total ice production of the Arctic Ocean. As the number of LKFs saturates for $N_{\mathrm{EVP}} > 550$, so does the SIV. Therefore, the mean SIV is a good indicator for the similarity between simulations that is simpler to diagnose than the number of LKFs. Similarly to the number of LKFs (Fig. 3), the differences in SIV between simulations are small for $N_{\mathrm{EVP}} > 550 - 650$.

Based on the analysis of LKFs and SIV, we choose N_{EVP}=550 as a practical compromise between quality of the sea ice simulation and computational performance. With sEVP and N_{EVP}=550 sea ice model code already uses almost the same amount of computational resources (80%) as the ocean model code. Further increase in N_{EVP} only leads to marginal changes in the number of LKFs and the SIV. N_{EVP}=550 is our reference value for the following experiments. Considerations of numerical stability lead to a similar estimate (see eq. A.22).

4 mEVP simulations

In the previous section we considered a series of simulations with different N_{EVP} values for the sEVP. For mEVP (Appendix A.4) we have to select α and β coefficients that ensure stability of the solution. Initial estimates of α and β can be obtained from expression (A.22), but these estimates need to be refined experimentally until sufficiently noise-free strain rates are obtained. Further increasing α and β beyond values that satisfy these criteria is not recommended as it would slow down convergence. The parameters α and β selected in this way are similar to the value of N_{EVP} for the sEVP.

For our setup with 4.5 km horizontal resolution in the Arctic Ocean we selected $\alpha = \beta = 500$. We performed five 10-years mEVP-experiments with the same parameter

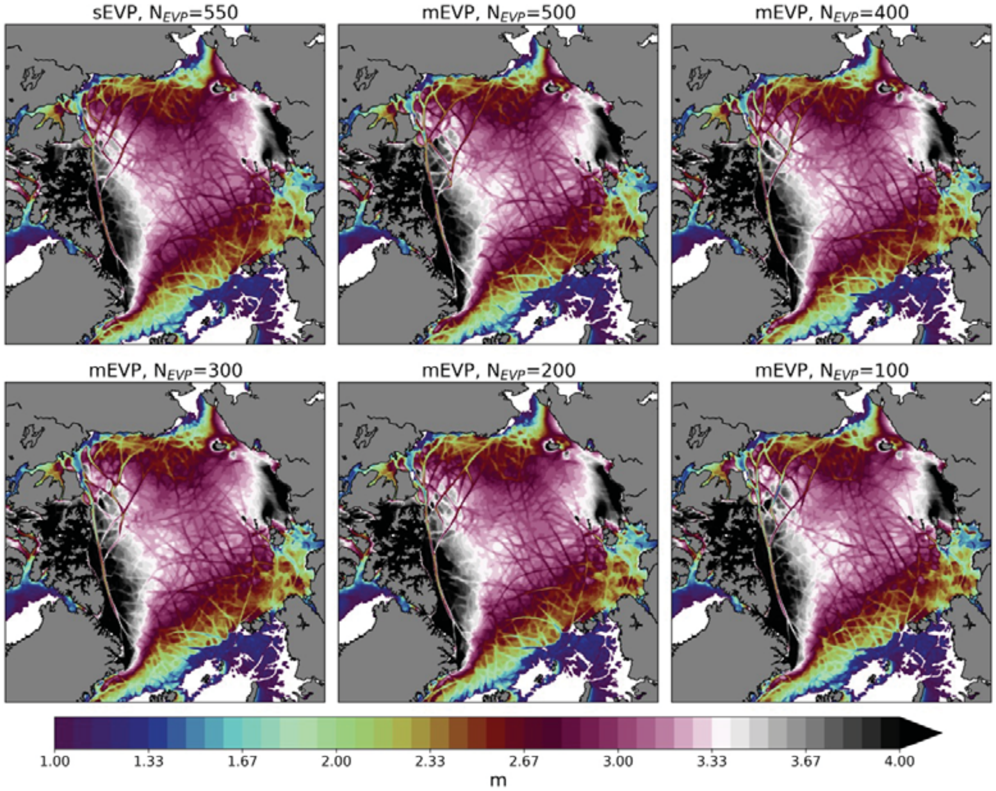

Figure 5. Snapshot of sea ice thickness on 31 December 1985 in sEVP and mEVP simulations (α and β = 500) with different values of N_{EVP}.

values as in the previous experiments with the sEVP, but with decreasing N_{EVP} from 500 to 100 in steps of 100. A further experiment with N_{EVP}=50 had unrealistic solutions with extremely thick sea ice and was discarded; as explained in the Appendix A.4, the number of sub-cycles (N_{EVP}) controls the convergence to the VP solution and after 50 sub-cycles the residuals in the EVP equations are not reduced sufficiently. The goal of these experiments is to find the lowest $\mathrm{N_{EVP}}$ that still leads to results comparable to the reference $\mathrm{N_{EVP}}$ = 550 with the sEVP.

In a comparison of the reference experiment (sEVP with N_{EVP} = 500) with mEVP solutions with different values of N_{EVP} on 31 December 1985 (Figure 5), the ice thickness fields differ in details of the LKF shape and distribution, but their large scale features are so similar that it is difficult to distinguish between the runs in terms of LKF density, length or other characteristics.

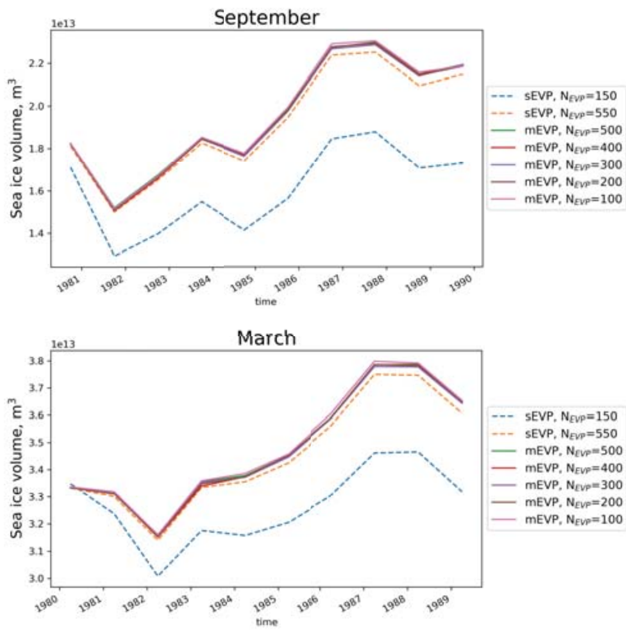

Figure 6. Monthly mean September (top) and March (bottom) sea ice volume in mEVP simulations with different values of N_{EVP} and with α and $\beta = 500$. Values of sEVP with $N_{\mathrm{EVP}} = 150$ and $N_{\mathrm{EVP}} = 550$ are also shown for reference.

We again use SIV as an indicator of similarity between simulations. Figure 6 shows mean September and March SIV for mEVP simulations with different values of N_{EVP}. The simulations with sEVP and N_{EVP} of 150 and 550 are also shown for comparison. All mEVP simulations show larger SIV compared to the sEVP simulations, while being close to the results of sEVP with $N_{\mathrm{EVP}} = 550$. Differences between the mEVP simulations are minimal and can be ignored in practice. One can conclude that with α and $\beta = 500$ and $\mathrm{N}_{\mathrm{EVP}}$=100, mEVP produces sea ice thickness fields that are close in visual characteristics and mean SIV values to sEVP simulations with at least $N_{\mathrm{EVP}} = 550$. For computational efficiency this means that sea ice dynamics can be calculated about six times faster without compromising the quality of the results.

5 aEVP simulations

The adaptive version of the solver aEVP (Appendix A.4) calculates the relaxation parameters α and β once per external time step as a function of local strain rates. A typical situation is that large values of α and β are only needed in small parts of the domain

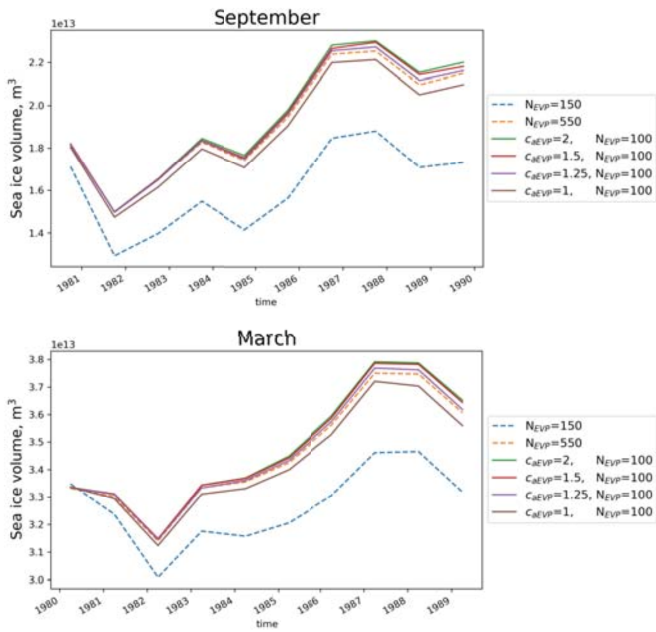

Figure 7. Monthly mean September (top) and March (bottom) sea ice volume in aEVP simulations with different values of c_{aEVP}. For aEVP, $\mathrm{N_{EVP}}$ = 100. Results for sEVP with $\mathrm{N_{EVP}}$=150 and $\mathrm{N_{EVP}}$=550 are shown for reference.

and that small values suffice everywhere else. The advantage of the aEVP solver is that it adaptively ensures stability in regions where stability is more difficult to achieve while converging faster than mEVP where the equations are less stiff [*Kimmritz et al.*, 2016, 2017] because lower values of α and β usually mean faster convergence. We have to adjust, however, a free-scaling parameter c_{aEVP} to the resolution of the mesh. If the values of α and β needed for stable performance of mEVP are already known, one selects c_{aEVP} so that peak values of α provided by (A.22) are close to the known values. Once again, the ultimate criterion is relatively small amount of noise in strain rates and viscosities.

For our 4.5 km mesh, we started with c_{aEVP} = 2.0 and gradually reduced this value to c_{aEVP} = 1.0. The configuration of the 10-years experiments with aEVP was the same as in the case of sEVP and mEVP, except that we used $\mathrm{N_{EVP}}$=100 for all experiments.

Figure 7 shows monthly mean September and March SIV for aEVP simulations with different c_{aEVP} as well as for sEVP simulations with N_{EVP} = 150 and N_{EVP} = 550 for comparison. The results are closest to those for sEVP with $\mathrm{N_{EVP}}$=550 for c_{aEVP}=1.25.

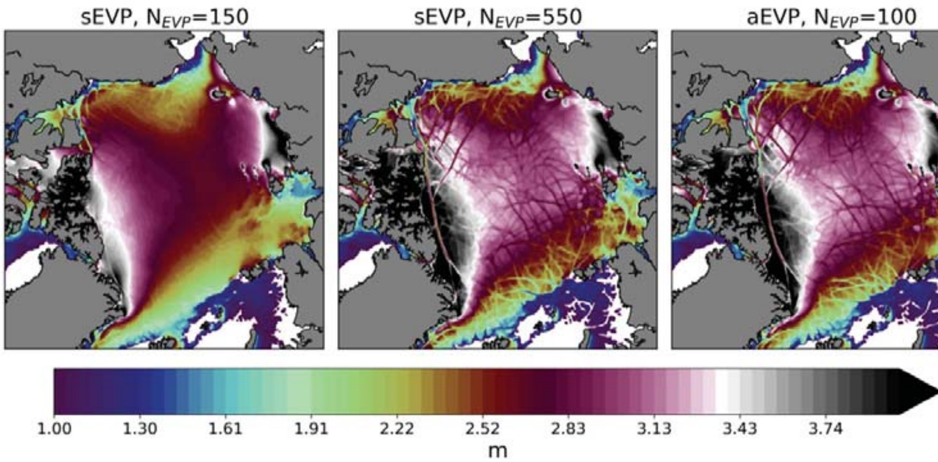

Figure 8. Snapshot of sea ice thickness in sEVP and aEVP simulations with different values of N_{EVP}

Larger values of c_{aEVP} lead to slightly larger values of SIV that, if compared to the sEVP results, would correspond to larger values of N_{EVP} (Fig. 4). For $c_{aEVP} = 1.5$, the average values for α and β are close to the constant α and β of the mEVP experiment. An optimal choice of c_{aEVP} would require more model tuning.

To summarize the results we show the sea ice thickness field after the aEVP tuning with $N_{EVP} = 100$ and $c_{aEVP} = 1.5$ together with results for the sEVP with 150 and 550 sub-cycles (Figure 8). The sea ice model with sEVP and $N_{EVP} = 150$ produces very smooth fields without LKFs. With $N_{EVP} = 100$, the aEVP solver produces a sea ice field that is similar to sEVP with $N_{EVP} = 550$.

6 Summary and conclusions

We use the unstructured mesh ocean model FESOM2 with FESIM as the sea ice component to explore the performance of the mEVP and aEVP solvers against the standard EVP (sEVP) solver in a realistic high-resolution setting. The model is set up on a global mesh with uniform 4.5 km refinement in the Arctic Ocean. The sEVP solver requires a large number (550 and more) of sub-cycles (N_{EVP}) to reach a practically satisfactory state where further increase of N_{EVP} does not dramatically change the spatial distribution of the sea ice thickness, in particular the presence of linear kinematic features (LKFs). With sEVP and $N_{EVP} = 550$ the computation of the sea ice dynamics uses 80% of the ocean model runtime. Using the mEVP and aEVP solvers allows us to have much smaller N_{EVP}=100, but still the characteristics of the sea ice field are close to those obtained with sEVP and $N_{\mathrm{EVP}} = 550$. This increases the computational efficiency of the sea ice code by a factor of 6, boosting the performance of FESOM2 on the particular mesh used here from a throughput of 25 simulated years per day with sEVP to 40 simulated years per day with mEVP on 1728 Intel®Xeon®Broadwell 2.3 GHz Cores.

The mEVP and aEVP solvers lead to results similar to the sEVP but with a reduced number of sub-cycles because the parameters that govern the stability of the solution on the one hand and its convergence to the VP dynamics on the other hand are clearly separated. By selecting appropriate parameters α and β the numerical procedure of mEVP and aEVP is made numerically stable. The number of sub-cycles is then chosen experimentally so that the noise in the deformation fields is reduced to an acceptable level. In practice that does not mean convergence (see Appendix A.5 for a brief discussion of convergence). If one determined the number of iterations based on residual reduction, the aEVP may be faster than mEVP because the residual is expected to be reduced faster in regions of small α and β [*Kimmritz et al.*, 2016].

This paper presents a practical example of tuning mEVP and aEVP solvers for a new configuration. The tuning exercise has several steps: (1) Finding appropriate parameter values α and β for mEVP. An initial guess is made as $\alpha = \beta = N_{\mathrm{EVP}}$ if a reasonable value of N_{EVP} that ensures stability of the sEVP algorithm is already known. Alternatively, an initial α and N_{EVP} can be determined based on a stability criterion (relation A.22), but this is less precise. After inspecting solutions for strain rates and viscosities for noise, this first guess may be adjusted to guarantee smooth solutions. (2) Finding the lowest possible N_{EVP} for mEVP. Starting from a sufficiently large $N_{\mathrm{EVP}} \geq \alpha$, N_{EVP} is reduced to the smallest value for which the deviation of the solutions from the run with high N_{EVP} is considered acceptable. (3) Adjusting c_{aEVP} for aEVP so that peak values are close to α and β needed for stability of mEVP.

We note that each new mesh may require additional tuning of the solver, in particular because the complexity of the solutions tends to increase with resolution. New forcing fields may also require additional tuning. For example, increased resolution of the wind forcing leads to stronger gradients in the wind stress which in turn increases the heterogeneity of sea-ice deformation [*Hutter*, 2015].

The presence of LKFs in the sea ice fields does not change significantly the total Arctic sea ice area (SIA), but leads to considerable changes in sea ice volume (SIV). Hence the sea ice thermodynamics may also need to be re-tuned in order to fit observations. Changes in the sea ice dynamics also lead to changes in the temperature and salinity fields [e.g. *Castellani et al.*, 2018]. These changes are strongest at the surface and may propagate as deep as the depth of the Atlantic Water layer. This also should be taken into account during the model tuning. We postpone these questions for future work.

Note that our experiments were performed under atmospheric forcing of the 1980s, and it remains to be seen if the tuning procedure will require additional steps in the low sea ice regime observed since the beginning of the 21^{st} century.

The advantages of the aEVP method over mEVP are not obvious in our simulations. For fixed N_{EVP} both methods require the same computer time. The expected improved convergence in areas with smaller α and β in aEVP is not visible in the simulated ice fields. However aEVP can become essential in setups with variable horizontal resolution where constant values of α and β may be a disadvantage.

We conclude that the mEVP and aEVP solvers increase the speed of the sea ice model calculations without compromising the quality of the simulated sea ice fields. This makes it possible to perform climate simulations with more realistic sea ice dynamics that start to resolve LKFs with a throughput of about 40 simulated years per day on the 4.5 km resolution mesh. At present our sea ice model uses the same CPUs that are used by the ocean model. Possible further optimization of the sea ice code in FESOM2 may involve using different mesh partitioning for sea ice and ocean and calculating sea ice dynamics not at every ocean time step.

A: The forms of EVP used with FESOM2

A.1 Sea ice dynamics

We briefly explain the equations of sea ice dynamics used in this study. The text below follows *Danilov et al.* [2015]. The 2D sea-ice momentum equation is

$$m(\partial_t + \mathbf{f}\times)\mathbf{u} = a\boldsymbol{\tau} - aC_d\rho_o(\mathbf{u}-\mathbf{u}_o)|\mathbf{u}-\mathbf{u}_o| + \mathbf{F} - mg\nabla H. \qquad \text{(A.1)}$$

In this equation $m = \rho_{ice}h_{ice} + \rho_s h_s$ is the total mass of ice plus snow per unit area, with densities ρ and mean thicknesses h over a grid cell (volumes per unit area), C_d is the ice-ocean drag coefficient, ρ_o is the water density, a is the sea ice concentration, $\mathbf{u} = (u, v)$ and $\mathbf{u}_o$ are the ice and ocean velocities, $\boldsymbol{\tau}$ is the wind stress applied to sea ice, H is the sea surface elevation, g is the acceleration due to gravity and $F_j = \partial_i \sigma_{ij}$ is the force from the internal stresses in ice. For brevity, we use Cartesian coordinates ($i, j = 1, 2$ correspond to x and y directions) and summation over repeating coordinate indices is implied.

The internal ice stresses for the VP rheology [*Hibler*, 1979] are written as

$$\sigma_{ij} = 2\eta\,(\dot\epsilon_{ij} - \frac{1}{2}\delta_{ij}\dot\epsilon_{kk}) + \zeta\delta_{ij}\dot\epsilon_{kk} - \frac{1}{2}\delta_{ij}P, \tag{A.2}$$

where

$$\dot\epsilon_{ij} = \frac{1}{2}\left(\frac{\partial u_i}{\partial x_j} + \frac{\partial u_j}{\partial x_i}\right) \tag{A.3}$$

is the strain rate tensor, η and ζ are the viscosities and P is the ice strength. We use the standard parameterization for the ice strength P and the expression for the viscosities η and ζ [*Hibler*, 1979]:

$$P = P_0, \quad \zeta = \frac{P_0}{2(\Delta + \Delta_{min})}, \quad \eta = \frac{\zeta}{e^2}, \tag{A.4}$$

where

$$P_0 = h_{ice} p^* e^{-C(1-a)}, \quad \Delta^2 = (\dot\epsilon_{11}^2 + \dot\epsilon_{22}^2)(1 + e^{-2}) + 4\dot\epsilon_{12}^2\, e^{-2} + 2\dot\epsilon_{11}\dot\epsilon_{22}(1 - e^{-2}), \tag{A.5}$$

with the FESOM default values $e = 2$, $C = 20$, $\Delta_{min} = 2 \cdot 10^{-9}$ s^{-1}, and $p^* = 27500$ N/m^2. Δ_{min} imposes a viscous regularization of plastic behavior in areas where Δ is very small. Replacement pressure [*Hibler and Ip*, 1995] is used, so that the ice strength is further modified as $P = P_0\Delta/(\Delta + \Delta_{min})$ to eliminate P in the absence of forcing.

A.2 Elastic-viscous-plastic approach

In the EVP approach [*Hunke and Dukowicz*, 1997, *Hunke and Lipscomb*, 2008], a pseudo-elastic term is added to the stress relation (A.2), so that the stress relaxes to the VP relation when elastic perturbations decay. Using

$$\sigma_1 = \sigma_{11} + \sigma_{22}, \quad \sigma_2 = \sigma_{11} - \sigma_{22} \tag{A.6}$$

and similar combinations for the strain rates

$$\dot\epsilon_1 = \dot\epsilon_{11} + \dot\epsilon_{22}, \quad \dot\epsilon_2 = \dot\epsilon_{11} - \dot\epsilon_{22}, \tag{A.7}$$

the EVP stress equations can be written as

$$\frac{\partial \sigma_1}{\partial t} + \frac{\sigma_1}{2T} = \frac{P_0}{2T(\Delta + \Delta_{min})}(\dot{\epsilon}_1 - \Delta), \tag{A.8}$$
$$\frac{\partial \sigma_2}{\partial t} + \frac{e^2\sigma_2}{2T} = \frac{P_0}{2T(\Delta + \Delta_{min})}\dot{\epsilon}_2, \tag{A.9}$$
$$\frac{\partial \sigma_{12}}{\partial t} + \frac{e^2\sigma_{12}}{2T} = \frac{P_0}{2T(\Delta + \Delta_{min})}\dot{\epsilon}_{12}, \tag{A.10}$$

where T is a relaxation time that determines the time scale of transition from elastic behavior to the VP rheology. The default value is $T = \Delta t/3$, where Δt is the external time step (set by the ocean model). The EVP stresses coincide with the VP ones if the contribution from the time derivatives are small towards the end of Δt.

The stress equations are stepped forward in time together with the momentum equation (A.1) with a short sub-cycling time step $\Delta t_{\mathrm{EVP}} = \Delta t/N_{\mathrm{EVP}}$, where N_{EVP} is the number of sub-cycles. Because the sub-cycling time step Δt_{EVP} is explicit, it is limited from above by numerical stability [see *Hunke and Dukowicz*, 1997, *Hunke*, 2001]. N_{EVP} is a large number. The CICE manual recommends 120 sub-cycles [*Hunke et al.*, 2010]. Assuming that Δt and hence T scales proportionally to the mesh resolution Δx, one expects that $N_{\mathrm{EVP}} \sim \Delta x^{-1/2}$. This places a restrictive upper limit on Δt_{EVP}, especially for fine meshes, and presents a problem for unstructured meshes with variable resolution. Failing to satisfy the upper limit on the sub-cycles time step generally leads to noise in the strain rates that modifies the solutions. In general, the fields of thickness and concentration remain comparably smooth.

A.3 EVP implementation of FESIM (sEVP)

A simple modification of the EVP equations strongly reduces the noise in ice strain rates [*Bouillon et al.*, 2013, *Danilov et al.*, 2015]. Dividing eqs. (A.9) and (A.10) by e^2, but neglecting this factor in the time derivatives, gives

$$\left(\frac{\partial}{\partial t} + \frac{1}{2T}\right)\sigma_1 = \frac{P_0}{2T(\Delta + \Delta_{min})}(\dot{\epsilon}_1 - \Delta), \tag{A.11}$$
$$\left(\frac{\partial}{\partial t} + \frac{1}{2T}\right)\sigma_2 = \frac{P_0}{e^2 2T(\Delta + \Delta_{min})}\dot{\epsilon}_2, \tag{A.12}$$
$$\left(\frac{\partial}{\partial t} + \frac{1}{2T}\right)\sigma_{12} = \frac{P_0}{e^2 2T(\Delta + \Delta_{min})}\dot{\epsilon}_{12}. \tag{A.13}$$

Note that for $\frac{\partial}{\partial t} \to 0$ one still recovers the VP expression for stresses. Our explanation of why (A.11–A.13) work better than (A.8–A.10) is that all three stress components approach their VP states at the same rate defined by $2T$. In the original formulation the rate is $2T$ for (A.8) and $2T/e^2$ for (A.9–A.10). The consequences of this modification are substantial, as illustrated in the supplementary material of *Wang et al.* [2016a]. This version is used in the standard EVP (sEVP) simulations in this study. Discretization with respect to time results in

$$\begin{aligned}
\frac{\sigma_1^{p+1}-\sigma_1^p}{\Delta t_{\mathrm{EVP}}}+\frac{\sigma_1^{p+1}}{2T} &= \frac{P_0^n}{2T(\Delta^p+\Delta_{min})}(\dot\epsilon_1^p-\Delta^p), && \text{(A.14)}\\
\frac{\sigma_2^{p+1}-\sigma_2^p}{\Delta t_{\mathrm{EVP}}}+\frac{\sigma_2^{p+1}}{2T} &= \frac{P_0^n}{e^2 2T(\Delta^p+\Delta_{min})}\dot\epsilon_2^p, && \text{(A.15)}\\
\frac{\sigma_{12}^{p+1}-\sigma_{12}^p}{\Delta t_{\mathrm{EVP}}}+\frac{\sigma_{12}^{p+1}}{2T} &= \frac{P_0^n}{e^2 2T(\Delta^p+\Delta_{min})}\dot\epsilon_{12}^p && \text{(A.16)}
\end{aligned}$$

for the stresses and

$$\begin{aligned}
\frac{\mathbf{u}^{p+1}-\mathbf{u}^p}{\Delta t_{\mathrm{EVP}}} &= -\mathbf{f}\times\mathbf{u}^{p+1}\\
&\quad+\frac{1}{m}[\mathbf{F}^{p+1}+a\boldsymbol{\tau}^n+C_d a\rho_o(\mathbf{u}_o^n-\mathbf{u}^{p+1})|\mathbf{u}_o^n-\mathbf{u}^p|-mg\nabla H^n] && \text{(A.17)}
\end{aligned}$$

for the velocity. Here n is the index of the external time step and $p=1,\ldots,N_{\mathrm{EVP}}$ is the index of sub-cycles. For $p=1$ fields are initialized with values at the external time level n, and their values for the last iteration $p=N_{\mathrm{EVP}}$ are taken as solutions for time level $n+1$.

A.4 Modified and adaptive EVP (mEVP and aEVP)

The modified EVP approach detaches sub-cycling from the physical time stepping [*Lemieux et al.*, 2012, *Bouillon et al.*, 2013, *Kimmritz et al.*, 2015]. Instead it can be seen as a pseudo-time solver for the VP rheology. The stress equations are rewritten as

$$\begin{aligned}
\alpha(\sigma_1^{p+1}-\sigma_1^p) &= \frac{P_0^n}{\Delta^p+\Delta_{\mathrm{min}}}(\dot\epsilon_1^p-\Delta^p)-\sigma_1^p, && \text{(A.18)}\\
\alpha(\sigma_2^{p+1}-\sigma_2^p) &= \frac{P_0^n}{(\Delta^p+\Delta_{\mathrm{min}})e^2}\dot\epsilon_2^p-\sigma_2^p, && \text{(A.19)}\\
\alpha(\sigma_{12}^{p+1}-\sigma_{12}^p) &= \frac{P_0^n}{(\Delta^p+\Delta_{\mathrm{min}})e^2}\dot\epsilon_{12}^p-\sigma_{12}^p, && \text{(A.20)}
\end{aligned}$$

and the momentum equation as

$$\begin{aligned}
\beta(\mathbf{u}^{p+1}-\mathbf{u}^p) &= -\mathbf{u}^{p+1}+\mathbf{u}^n-\Delta t\mathbf{f}\times\mathbf{u}^{p+1}\\
&\quad+\frac{\Delta t}{m}[\mathbf{F}^{p+1}+a\boldsymbol{\tau}+C_d a\rho_o(\mathbf{u}_o^n-\mathbf{u}^{p+1})|\mathbf{u}_o^n-\mathbf{u}^p|-mg\nabla H^n]. && \text{(A.21)}
\end{aligned}$$

Here α and β are some large constants. The superscript p denotes the pseudo-time iterations, replacing the sub-cycling of the standard EVP, and n is the index of the external time level. Fields are initialized with values at the external time level n for $p = 1$, and their values for the last iteration $p = N_{EVP}$ are taken as solutions for time level $n+1$.

For iterations to be stable, the product $\alpha\beta$ should be sufficiently large compared to $\pi^2 P_0 \Delta t(\Delta + \Delta_{\min})^{-1} m^{-1} \Delta x^{-2}$ [*Bouillon et al.*, 2013, *Kimmritz et al.*, 2015]. A comment on the relation between the parameters of sEVP and mEVP seems in place. Comparing, for example, (A.11) and (A.18) we see that $2T$ in sEVP is similar to $\alpha\Delta t_{\mathrm{EVP}} = \alpha\Delta t/N_{\mathrm{EVP}}$ in mEVP. The common selection $T = \Delta t/3$ in sEVP then implies that $\alpha = (2/3)N_{\mathrm{EVP}}$. The relaxation toward the VP stresses follows $\exp(t/2T)$ in sEVP and $\exp(-p/\alpha)$ in mEVP and for $T = \Delta t/3$ both lead to the attenuation factor $e^{-3/2}$ by the end of the time step Δt. For given α, the number of sub-cycles N_{EVP} in mEVP defines how far the VP state is approached per external time step. The sEVP scheme with $N_{\mathrm{EVP}} = 120$ and $T = \Delta t/3$ approximately corresponds to $\alpha = \beta = 80$ in mEVP if N_{EVP} is kept the same and neglecting all stability considerations. Although stability requirements are similar for sEVP and mEVP if expressed in equivalent terms, stability is governed by the selection of α and β in mEVP, and is not related to N_{EVP}. This difference is of primary importance because it governs how N_{EVP} is determined: After selecting α and β so that stability is ensured, one starts with N_{EVP} well in excess of α and β and reduces it in a set of runs to find the smallest possible value. Once found for a particular resolution, it is hoped that the parameters are suitable for all other setups at this resolution. Note that while the stress equations in sEVP and mEVP can be made identical by adjusting the notation, the momentum equations differ in the treatment of the time derivative. All simulations were performed with $\alpha = \beta$.

The adaptive method makes one further step by estimating α and β at each particular location at run time [*Kimmritz et al.*, 2016]. We use

$$\alpha = \max\left(50, c_{\mathrm{aEVP}}\sqrt{\frac{P_0\Delta t}{(\Delta + \Delta_{min})\, m A_c}}\right), \tag{A.22}$$

at each triangular cell. In this expression A_c is the area of the triangular mesh cell. The constant c_{aEVP} needs to be determined experimentally, because c_{aEVP}/A_c is an estimate for the unknown eigenvalues of the second-order differential operator stemming from the divergence of stresses [*Kimmritz et al.*, 2016]. Once the field of α is known at triangles, we determine β at mesh vertices (where velocities are taken) by looking for the maximum α on neighboring triangles. The complexity of the solutions increases with resolution because of an increased amount of simulated LKFs. This is the reason why an adjustment of c_{aEVP} may be needed.

Note that with $c_{\mathrm{aEVP}} = 1$, (A.22) can be used for a guess for the value of $\alpha = \beta$ needed for stability of mEVP. For our 4.5 km mesh $A_c \approx 2 \times 10^7$ m^2, so the estimate is $\alpha \approx 800$ for the worst case of very small Δ. A slightly smaller value of $\alpha = 500$ was found to already ensure nearly noise-free sea ice fields in our simulations.

We also note that the particular values of the parameters may depend on details of the discretization, but we do not expect large deviations from the values reported here for the FESIM implementation of the considered EVP solvers.

A.5 Comments on the convergence of mEVP and aEVP

Kimmritz et al. [2017] compared the accuracy and convergence of mEVP and aEVP with respect to the numerically converging solutions obtained with a JFNK solver in a realistic Arctic configuration with a resolution of 27 km and the Massachusetts Institute of Technology general circulation model [*Marshall et al.*, 1997]. They concluded that the difference between the mEVP (aEVP) and JFNK solutions is negligible from a practical point of view. Note, however, that they found convergence of mEVP (aEVP) only without using the replacement pressure (RP) method, while the convergence stalled with RP. The fields of residuals defined as the left hand sides of (A.18-A.20) and (A.21) showed a wave-like pattern propagating from the area of the Canadian Archipelago in the RP case, yet it was found to have little bearing on the agreement with the JFNK solution. The behavior of FESIM is very similar at the similar 25 km resolution (not shown), but also at the resolution of 4.5 km used here (Fig. A.1).

Using $\alpha, \beta = 500$ for our 4.5 km configuration represents a compromise and still leaves a small area with noise in the field of Δ that we used for diagnostics (not shown). Because of this noise, true convergence, judged by the behavior of the area-mean L^2 norm of the residuals (Figure A.1), is not achieved independent of the RP, and $N_{\mathrm{EVP}} = 100$ ensures only a small error reduction. The noise fully disappears for $\alpha, \beta = 1700$, which allows a residual norm reduction by about 12 orders of magnitudes in the no RP case for $N_{\mathrm{EVP}} = 50000$, which agrees with the exponential scaling $(\exp(-p/\alpha))$. This number of iterative steps is impractically high.

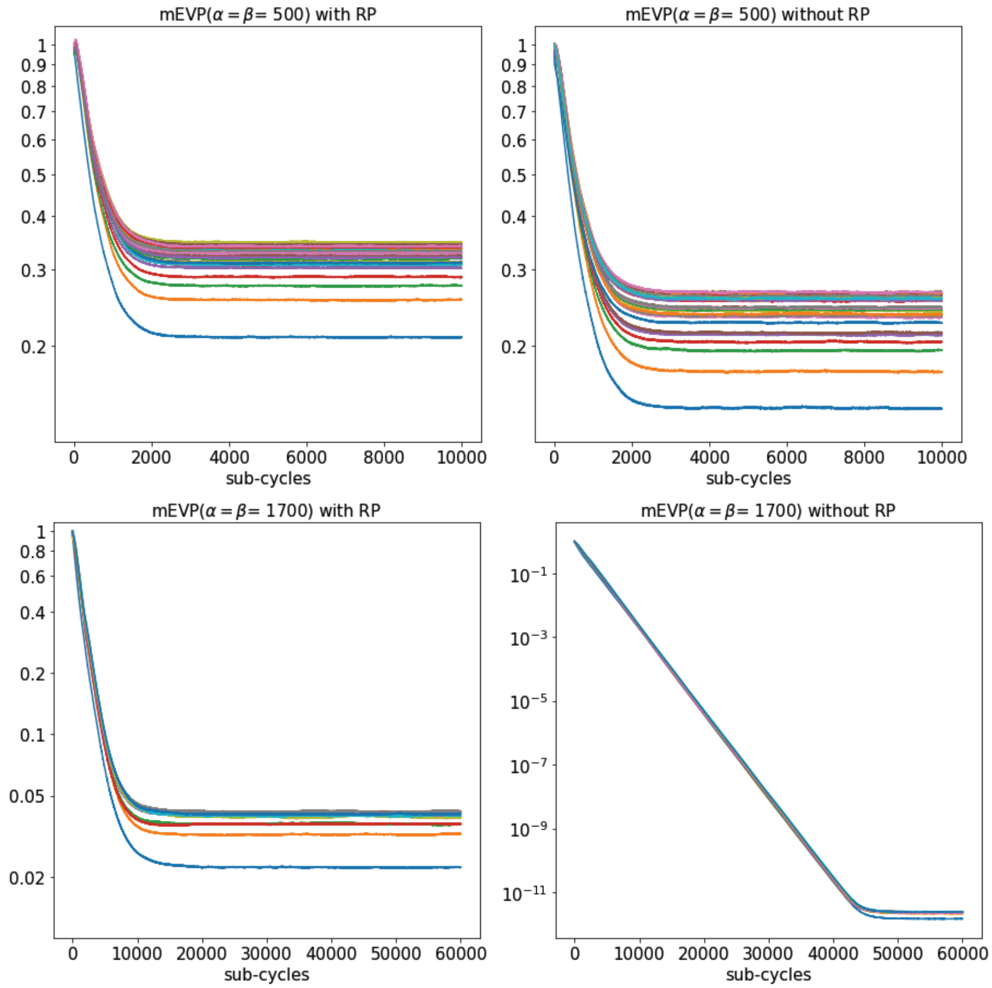

Figure A.1. Area-mean L^2 norm of the residuals with (left) and without replacement pressure (right), using $\alpha, \beta = 500$ (top) and $\alpha, \beta = 1700$ (bottom). Different colors denote randomly selected different ocean (external) time levels.

Practically affordable EVP solutions stay therefore very far from convergence to the VP rheology. Based on the results of *Kimmritz et al.* [2017] we can hope that the simulated ice thickness distribution is close to the hypothetical VP solution. Yet we cannot draw such conclusions based on the distribution of LKFs (Fig. 2, 4) because there are no analogous feature in the coarse resolution simulations of [*Kimmritz et al.*, 2017]. We do not see any essential changes in the sea-ice thickness distribution and the number of simulated LKFs with mEVP for the range of parameters explored, but N_{EVP} is still far from values needed for convergence. Pseudo-elastic waves are present in such solutions and may affect the distribution of simulated LKFs.

To explore the question of how much convergence is "necessary" with EVP, comparisons with solutions obtained with a Picard solver, and with converged EVP solution with larger α and very large N_{EVP} are required. Typically a Picard solver with order 10 iterations also does not converge, but it is free of pseudo-elastic waves. The converged mEVP solutions can be simulated for limited time intervals despite their rather high cost. The Picard solver of FESIM is still not adapted to FESOM2. Respective results will be presented in due course.

Acknowledgments

We thank Jean-François Lemieux and anonymous reviewer for their very helpful comments. This paper is a contribution to the projects S1 (Diagnosis and Metrics in Climate Models) and S2 (Improved parameterisations and numerics in climate models) of the Collaborative Research Centre TRR 181 "Energy Transfer in Atmosphere and Ocean" funded by the Deutsche Forschungsgemeinschaft (DFG, German Research Foundation) - Projektnummer 274762653 (N. Koldunov, S. Danilov, P. Scholz, T. Jung). It is also supported by the EC project PRIMAVERA under the grant agreement no. 641727 (D. Sein, T. Jung), by the Helmholtz Climate Initiative REKLIM (Regional Climate Change) (D. Sidorenko and Q. Wang), the state assignment of FASO Russia (theme 0149-2018-001) and by the ERA-Net projects EXOSYSTEM (grant agreement 01DJ16016) and FRAGERUS (grant agreement 01DJ15029) funded by the Federal Ministry for Education and Research (Germany). H. Goessling acknowledges SSIP funding by the Federal Ministry for Education and Research (grant 01LN1701A). The data are available at `https://swiftbrowser.dkrz.de/public/dkrz_035d8f6ff058403bb42f8302e6badfbc/Koldunov_EVP_2018/`. Stable version of FESOM2 code is available at `https://github.com/FESOM/fesom2`.

References

Bouchat, A., and B. Tremblay (2017), Using sea-ice deformation fields to constrain the mechanical strength parameters of geophysical sea ice, *Journal of Geophysical Research: Oceans*, *122*(7), 5802–5825.

Bouillon, S., T. Fichefet, V. Legat, and G. Madec (2013), The elastic-viscous-plastic method revisited, *Ocean Modelling*, *71*, 2–12.

Castellani, G., M. Losch, M. Ungermann, and R. Gerdes (2018), Sea-ice drag as a function of deformation and ice cover: Effects on simulated sea ice and ocean circulation in the Arctic., *Ocean Modelling*.

Coon, M., R. Kwok, G. Levy, M. Pruis, H. Schreyer, and D. Sulsky (2007), Arctic ice dynamics joint experiment (AIDJEX) assumptions revisited and found inadequate, *Journal of Geophysical Research: Oceans*, *112*(C11).

Danilov, S., Q. Wang, R. Timmermann, N. Iakovlev, D. Sidorenko, M. Kimmritz, T. Jung, and J. Schröter (2015), Finite-element sea ice model (FESIM), version 2, *Geoscientific Model Development*, *8*(6), 1747–1761.

Danilov, S., D. Sidorenko, Q. Wang, and T. Jung (2017), The Finite-volumE Sea ice–Ocean Model (FESOM2), *Geosci. Model Dev.*, *10*, 765–789.

Dansereau, V., J. Weiss, P. Saramito, and P. Lattes (2016), A Maxwell elasto-brittle rheology for sea ice modelling, *The Cryosphere*, *10*(3), 1339–1359.

Ernsdorf, T., D. Schröder, S. Adams, G. Heinemann, R. Timmermann, and S. Danilov (2011), Impact of atmospheric forcing data on simulations of the laptev sea polynya dynamics using the sea-ice ocean model FESOM, *Journal of Geophysical Research: Oceans*, *116*(C12).

Gent, P. R., and J. C. Mcwilliams (1990), Isopycnal mixing in ocean circulation models, *Journal of Physical Oceanography*, *20*(1), 150–155.

Girard, L., S. Bouillon, J. Weiss, D. Amitrano, T. Fichefet, and V. Legat (2011), A new modeling framework for sea-ice mechanics based on elasto-brittle rheology, *Annals of Glaciology*, *52*(57), 123–132.

Herman, A. (2011), Molecular-dynamics simulation of clustering processes in sea-ice floes, *Physical Review E*, *84*(5), 056,104.

Hibler, W., and E. M. Schulson (2000), On modeling the anisotropic failure and flow of flawed sea ice, *Journal of Geophysical Research: Oceans*, *105*(C7), 17,105–17,120.

Hibler, W. D., III (1979), A Dynamic Thermodynamic Sea Ice Model, *J. Phys. Oceanogr.*, *9*, 815–846.

Hibler, W. D., III, and C. F. Ip (1995), The effect of sea ice rheology on Arctic buoy drift, *J. P. Dempsey and Y. D. S. Rajapakse (eds.) ASME AMD*, *207, Ice Mechanics*, 255–263.

Hopkins, M. A. (2004), A discrete element Lagrangian sea ice model, *Engineering Computations*, *21*(2/3/4), 409–421.

Hoyer, S., and J. Hamman (2017), xarray: N-D labeled arrays and datasets in Python, *Journal of Open Research Software*, *5*(1), doi:10.5334/jors.148.

Hunke, E., and W. Lipscomb (2008), CICE: The Los Alamos sea ice model documentation and software userâĂŹs manual. Tech. Rep., *T-3 Fluid Dynamics Group, Los Alamos National Laboratory, Los Alamos NM 87545*.

Hunke, E. C. (2001), Viscous-plastic sea ice dynamics with the EVP model: Linearization issues, *J. Comp. Phys.*, *170*, 18–38.

Hunke, E. C., and J. K. Dukowicz (1997), An Elastic-Viscous-Plastic model for sea ice dynamics, *J. Phys. Oceanogr.*, *27*, 1849–1867.

Hunke, E. C., W. H. Lipscomb, A. K. Turner, N. Jeffery, and S. Elliott (2010), CICE: the Los Alamos sea ice model documentation and software userâĂŹs manual version 4.1 la-cc-06-012, *T-3 Fluid Dynamics Group, Los Alamos National Laboratory*, *675*.

Hunter, J. D. (2007), Matplotlib: A 2D graphics environment, *Computing In Science & Engineering*, *9*(3), 90–95, doi:10.1109/MCSE.2007.55.

Hutter, N. (2015), Viscous-plastic sea-ice models at very high resolution, Master's thesis, University of Bremen, Alfred Wegener Institute, Helmholtz Centre for Polar and Marine research, doi:10013/epic.46129.

Hutter, N., M. Losch, and D. Menemenlis (2018a), Scaling properties of Arctic sea ice deformation in a high-resolution viscous-plastic sea ice model and in satellite observations, *Journal of Geophysical Research: Oceans*, *123*(1), 672–687, doi:10.1002/2017JC013119.

Hutter, N., L. Zampieri, and M. Losch (2018b), Leads and ridges in Arctic sea ice from rgps data and a new tracking algorithm, *The Cryosphere Discussions*, *2018*, 1–27, doi:10.5194/tc-2018-207.

Kimmritz, M., S. Danilov, and M. Losch (2015), On the convergence of the modified elastic-viscous-plastic method for solving the sea ice momentum equation, *J. Comp. Phys.*, *296*, 90–100.

Kimmritz, M., S. Danilov, and M. Losch (2016), The adaptive EVP method for solving the sea ice momentum equation, *Ocean Modelling*, pp. –, doi:http://dx.doi.org/10.1016/j.ocemod.2016.03.004.

Kimmritz, M., M. Losch, and S. Danilov (2017), A comparison of viscous-plastic sea ice solvers with and without replacement pressure, *Ocean Modelling*, *115*, 59–69.

Kluyver, T., B. Ragan-Kelley, F. Pérez, B. Granger, M. Bussonnier, J. Frederic, K. Kelley, J. Hamrick, J. Grout, S. Corlay, P. Ivanov, D. Avila, S. Abdalla, and C. Willing (2016), Jupyter notebooks – a publishing format for reproducible computational workflows, in *Positioning and Power in Academic Publishing: Players, Agents and Agendas*, edited by F. Loizides and B. Schmidt, pp. 87 – 90, IOS Press.

Koldunov, N. V., D. Stammer, and J. Marotzke (2010), Present-day arctic sea ice variability in the coupled ECHAM5/MPI-OM model, *Journal of Climate*, *23*(10), 2520–2543.

Kwok, R. (2006), Contrasts in sea ice deformation and production in the arctic seasonal and perennial ice zones, *Journal of Geophysical Research: Oceans*, *111*(C11).

Large, W. G., and S. Yeager (2009), The global climatology of an interannually varying air–sea flux data set, *Climate dynamics*, *33*(2-3), 341–364.

Large, W. G., J. C. McWilliams, and S. C. Doney (1994), Oceanic vertical mixing: A review and a model with a nonlocal boundary layer parameterization, *Reviews of Geophysics*, *32*(4), 363–403.

Lemieux, J.-F., D. Knoll, B. Tremblay, D. Holland, and M. Losch (2012), A comparison of the Jacobian-free Newton-Krylov method and the EVP model for solving the sea ice momentum equation with a viscous-plastic formulation: a serial algorithm study, *J. Comp. Phys.*, *231*(17), 5926–5944.

Linow, S., and W. Dierking (2017), Object-based detection of Linear Kinematic Features in sea ice, *Remote Sensing*, *9*(5), doi:10.3390/rs9050493.

Losch, M., and S. Danilov (2012), On solving the momentum equations of dynamic sea ice models with implicit solvers and the elasticâĂŞviscousâĂŞplastic technique, *Ocean Modelling*, *41*, 42–52.

Losch, M., D. Menemenlis, J.-M. Campin, P. Heimbach, and C. Hill (2010), On the formulation of sea-ice models. Part 1: Effects of different solver implementations and parameterizations, *Ocean Modelling*, *3*(1–2), 129–144.

Losch, M., A. Fuchs, J.-F. Lemieux, and A. Vanselow (2014), A parallel Jacobian-free NewtonâĂŞKrylov solver for a coupled sea ice-ocean model, *J. Comp. Phys.*, *257, Part A*(0), 901–911.

Marshall, J., A. Adcroft, C. Hill, L. Perelman, and C. Heisey (1997), A finite-volume, incompressible Navier Stokes model for studies of the ocean on parallel computers, *Journal of Geophysical Research: Oceans*, *102*(C3), 5753–5766.

McKinney, W. (2010), Data structures for statistical computing in python, in *Proceedings of the 9th Python in Science Conference*, edited by S. van der Walt and J. Millman, pp. 51 – 56.

Rampal, P., J. Weiss, D. Marsan, R. Lindsay, and H. Stern (2008), Scaling properties of sea ice deformation from buoy dispersion analysis, *Journal of Geophysical Research: Oceans*, *113*(C3).

Rampal, P., S. Bouillon, E. Ólason, and M. Morlighem (2016), neXtSIM: a new lagrangian sea ice model, *The Cryosphere*, *10*(3), 1055–1073, doi:10.5194/tc-10-1055-2016.

Redi, M. H. (1982), Oceanic isopycnal mixing by coordinate rotation, *Journal of Physical Oceanography*, *12*(10), 1154–1158.

Ringeisen, D., N. Hutter, M. Losch, and L. B. Tremblay (2018), Modeling sea ice fracture at very high resolution with VP rheologies, *The Cryosphere Discussions*, *2018*, 1–28, doi:10.5194/tc-2018-192.

Sein, D. V., S. Danilov, A. Biastoch, J. V. Durgadoo, D. Sidorenko, S. Harig, and Q. Wang (2016), Designing variable ocean model resolution based on the observed ocean variability, *Journal of Advances in Modeling Earth Systems*, *8*(2), 904–916.

Sein, D. V., N. V. Koldunov, S. Danilov, Q. Wang, D. Sidorenko, I. Fast, T. Rackow, W. Cabos, and T. Jung (2017), Ocean modeling on a mesh with resolution following the local Rossby radius, *Journal of Advances in Modeling Earth Systems*, *9*(7), 2601–2614.

Semtner Jr, A. J. (1976), A model for the thermodynamic growth of sea ice in numerical investigations of climate, *Journal of Physical Oceanography*, *6*(3), 379–389.

Spreen, G., R. Kwok, D. Menemenlis, and A. T. Nguyen (2017), Sea-ice deformation in a coupled ocean–sea-ice model and in satellite remote sensing data, *The Cryosphere*, *11*(4), 1553–1573, doi:10.5194/tc-11-1553-2017.

Steele, M., R. Morley, and W. Ermold (2001), PHC: a global ocean hydrography with a high-quality Arctic Ocean, *Journal of Climate*, *14*(9), 2079–2087.

Stroeve, J., A. Barrett, M. Serreze, and A. Schweiger (2014), Using records from submarine, aircraft and satellites to evaluate climate model simulations of Arctic sea ice thickness, *The Cryosphere*, *8*(5), 1839–1854, doi:10.5194/tc-8-1839-2014.

Tremblay, L., and L. Mysak (1997), Modeling sea ice as a granular material, including the dilatancy effect, *Journal of Physical Oceanography*, *27*(11), 2342–2360.

Tsamados, M., D. L. Feltham, and A. Wilchinsky (2013), Impact of a new anisotropic rheology on simulations of Arctic sea ice, *Journal of Geophysical Research: Oceans*, *118*(1), 91–107.

Van der Walt, S., J. L. Schönberger, J. Nunez-Iglesias, F. Boulogne, J. D. Warner, N. Yager, E. Gouillart, and T. Yu (2014), scikit-image: image processing in python, *PeerJ*, *2*, e453.

Wang, Q., S. Danilov, D. Sidorenko, R. Timmermann, C. Wekerle, X. Wang, T. Jung, and J. Schröter (2014), The Finite Element Sea Ice-Ocean model (FESOM) v. 1.4: formulation of an ocean general circulation model, *Geoscientific Model Development*, *7*(2), 663–693.

Wang, Q., S. Danilov, T. Jung, L. Kaleschke, and A. Wernecke (2016a), Sea ice leads in the Arctic Ocean: Model assessment, interannual variability and trends, *Geophysical Research Letters*, *43*(13), 7019–7027.

Wang, Q., M. Ilicak, R. Gerdes, H. Drange, Y. Aksenov, D. A. Bailey, M. Bentsen, A. Biastoch, A. Bozec, C. Böning, et al. (2016b), An assessment of the Arctic Ocean in a suite of interannual CORE-II simulations. Part I: Sea ice and solid freshwater, *Ocean Modelling*, *99*, 110–132.

Wang, Q., C. Wekerle, S. Danilov, X. Wang, and T. Jung (2018a), A 4.5 km resolution Arctic Ocean simulation with the global multi-resolution model FESOM1. 4, *Geosci. Model Dev.*, *11*, 1229–1255.

Wang, Q., C. Wekerle, S. Danilov, N. Koldunov, D. Sidorenko, D. Sein, B. Rabe, and T. Jung (2018b), Arctic sea ice decline significantly contributed to the unprecedented liquid freshwater accumulation in the Beaufort Gyre of the Arctic Ocean, *Geophysical Research Letters*.

Wang, Q., C. Wekerle, S. Danilov, D. Sidorenko, N. Koldunov, D. Sein, B. Rabe, and T. Jung (2019), Recent sea ice decline did not significantly increase the total liquid freshwater content of the Arctic Ocean, *Journal of Climate*, *32*(1), 15–32.

Weiss, J., E. M. Schulson, and H. L. Stern (2007), Sea ice rheology from in-situ, satellite and laboratory observations: Fracture and friction, *Earth and Planetary Science Letters*, *255*(1-2), 1–8.

Wekerle, C., Q. Wang, W.-J. von Appen, S. Danilov, V. Schourup-Kristensen, and T. Jung (2017a), Eddy-resolving simulation of the Atlantic Water circulation in the Fram Strait with focus on the seasonal cycle, *Journal of Geophysical Research: Oceans*, *122*(11), 8385–8405.

Wekerle, C., Q. Wang, S. Danilov, V. Schourup-Kristensen, W.-J. von Appen, and T. Jung (2017b), Atlantic Water in the Nordic Seas: Locally eddy-permitting ocean simulation in a global setup, *Journal of Geophysical Research: Oceans*, *122*(2), 914–940.

Wilchinsky, A. V., and D. L. Feltham (2012), Rheology of discrete failure regimes of anisotropic sea ice, *Journal of physical oceanography*, *42*(7), 1065–1082.

Zhang, J., and W. Hibler (1997), On an efficient numerical method for modeling sea ice dynamics, *J. Geophys. Res.*, *102*, 8691–8702.

Zhang, J., and D. Rothrock (2005), Effect of sea ice rheology in numerical investigations of climate, *Journal of Geophysical Research: Oceans*, *110*(C8).